Radiological Physics and Technology (2019) 12:105–117
https://doi.org/10.1007/s12194-018-00497-0

Simulation of photon-counting detectors for conversion of dual-energy-subtracted computed tomography number to electron density

Masatoshi Saito[1]

Received: 7 December 2017 / Revised: 29 December 2018 / Accepted: 29 December 2018 / Published online: 9 January 2019

Abstract
For accurate tissue-inhomogeneity correction in radiotherapy treatment planning, the author previously proposed a conversion of the energy-subtracted computed tomography (CT) number to electron density (ΔHU–ρ_e conversion). The purpose of the present study was to provide a method for investigating the accuracy of a photon-counting detector (PCD) used in the ΔHU–ρ_e conversion by performing dual-energy CT image simulations of a PCD system with two energy bins. To optimize the tube voltage and threshold energy, the image noise and errors in ρ_e calibration were evaluated using three types of virtual phantoms: a 35-cm-diameter pure water phantom, 33-cm-diameter solid water surrogate phantom equipped with 16 inserts, and another solid water surrogate phantom with a 25-cm diameter. The third phantom was used to investigate the effect of the object's size on the ρ_e-calibration accuracy of PCDs. Two different scenarios for the PCD energy response were considered, corresponding to the ideal and realistic cases. In addition, a simple correction method for improving the spectral separation of the dual energies in a realistic PCD was proposed to compensate for its performance loss. In the realistic PCD case, there exists a trade-off between the image noise and ρ_e-calibration errors. Furthermore, the weakest image noise was nearly twice that for the ideal case, and the ρ_e-calibration error did not reach practical levels for any threshold energy. Nevertheless, the proposed correction method is likely to decrease the ρ_e-calibration errors of a realistic PCD to the level of the ideal case, yielding more accurate ρ_e values that are less affected by object size variation.

Keywords Photon-counting detector · Electron density · Dual-energy CT · Energy-selective CT

1 Introduction

The correction of tissue inhomogeneity, achieved by converting the computed tomography (CT) number (in Hounsfield units, HU) into an electron density relative to water (ρ_e), is one of the key procedures that determine the accuracy of patient dose calculations in radiotherapy treatment planning (RTP) [1]. Although the HU–ρ_e conversion is usually performed using tissue substitutes with known electron densities in a calibration phantom [2], the elemental composition of those tissue substitutes differs from that of real tissues; consequently, inappropriate calibration curves may be used for the HU–ρ_e conversion. To avoid this problem, a stoichiometric calibration method was introduced by Schneider et al. [3]. This method may provide better results compared with the conventional tissue-substitute calibration method. However, even if such calibration is performed successfully, the CT number and ρ_e of tissues cannot be in one-to-one correspondence, because the CT numbers estimated from the attenuation coefficients depend on the electron densities and effective atomic numbers. Accordingly, the CT numbers of tissues with equal electron density can vary because of their different effective atomic numbers [4].

To overcome this difficulty in the ρ_e calibration, the author previously proposed a dual-energy (DE) application for converting the energy-subtracted CT number (ΔHU) to an electron-density value (hereafter referred to as the ΔHU–ρ_e conversion), in which there exists an excellent linear relationship between ΔHU and ρ_e over a wide range of ρ_e [5]. Although the ΔHU–ρ_e conversion can be inherently performed using any existing single-source or dual-source DE CT (DECT) scanner, thus far, the accuracy of the ΔHU–ρ_e conversion has been investigated primarily using dual-source CT (DSCT) scanners [6–9]. This is because a tin

✉ Masatoshi Saito
masaito@clg.niigata-u.ac.jp

[1] Department of Radiological Technology, School of Health Sciences, Faculty of Medicine, Niigata University, Niigata 951-8518, Japan

filter attached to the high-kV tube of a DSCT scanner yields a larger spectral separation of dual energies [10], resulting in more accurate ρ_e calibration that is less affected by variations in the object's size [6, 7]. Unfortunately, the scan field of view (SFOV) of DSCT scanners in the DE mode is limited to a maximum diameter of 35 cm. This limited SFOV is likely to be problematic in RTP, because the SFOV needs to fully cover the patient's body on the image, along with all immobilization devices that might be penetrated by the therapy beam.

An energy-selective photon-counting detector (PCD), known to be a promising candidate for use in next-generation CT systems [11, 12], would be the most suitable modality for applying the ΔHU–ρ_e conversion. Using this type of detector, the X-ray energy spectrum can be split into several energy bins, and multi-energy CT images can be acquired at a fixed tube voltage in a single CT scan. PCDs offer potential benefits that include higher image quality, lower dose, and the ability to differentiate multiple *K*-edge contrast agents, which result from reduced electronic noise, higher detection efficiency, and energy discrimination capability in a single data-acquisition step without an overlap in the X-ray spectrum. This also allows multi-energy CT to be performed in the full range of SFOV (> 50 cm) and prevents cross-scattered radiation and mis-registration artifacts that can occur when using DSCT scanners to acquire high- and low-energy data sets, with a mechanical offset of ~ 90°.

The main objective of this study was to investigate the performance of a PCD in terms of its accuracy for the ΔHU–ρ_e conversion by simulating CT images. This paper describes a method for the optimization of spectral parameters, tube voltage, and threshold energy, which minimizes the image noise as well as errors in the ρ_e calibration. Two different scenarios for the energy response of PCDs are considered, corresponding to the ideal and realistic cases [13]. In addition, a very simple method for improving the spectral separation of a realistic PCD is proposed to compensate for its performance loss.

2 Materials and methods

2.1 The ΔHU–ρ_e conversion method

Below, the ΔHU–ρ_e conversion method is briefly reviewed [5]. We introduce a DE-subtracted quantity, ΔHU, into the ρ_e calibration, which is defined as follows:

$$\Delta\mathrm{HU} \equiv (1+\alpha)\mathrm{HU_H} - \alpha\mathrm{HU_L}. \tag{1}$$

Here, HU_k is the CT number in Hounsfield units for high-energy ($k = \mathrm{H}$) and low-energy ($k = \mathrm{L}$) scans and α is the weighting factor for the subtraction, specified only by the mean energy difference between the high-energy and low-energy spectra of a CT scanner. For materials with low effective atomic numbers, we can expect the relationship between ΔHU and ρ_e to be invariably linear [14]. Using a ΔHU–ρ_e data set derived from DECT scans of materials with known ρ_e values in a calibration phantom, the weighting factor α is determined from the least-squares fit of a linear function for the calibrated ρ_e, i.e., ρ_e^{cal}, as follows:

$$\rho_e^{\mathrm{cal}} = \frac{\Delta\mathrm{HU}}{1000} + 1. \tag{2}$$

The weighting factor α can be expressed as follows based on Eqs. (1) and (2) using the definition of the CT number:

$$\alpha = \frac{1}{\frac{\frac{\mu_\mathrm{L}}{\mu_\mathrm{L}^\mathrm{w}} - \rho_e}{\frac{\mu_\mathrm{H}}{\mu_\mathrm{H}^\mathrm{w}} - \rho_e} - 1}, \tag{3}$$

where μ_k and μ_k^w ($k = \mathrm{L}, \mathrm{H}$) are the linear attenuation coefficients of the material and water, respectively. A previous study proved that α can be regarded as an almost material-independent parameter [5]. This equation suggests that a greater difference between $\mu_\mathrm{L}/\mu_\mathrm{L}^\mathrm{w}$ and $\mu_\mathrm{H}/\mu_\mathrm{H}^\mathrm{w}$, i.e., a greater spectral separation between the dual X-ray energies, leads to a smaller α value. Figure 1 schematically shows the workflow of the DECT-image-based RTP. The ΔHU–ρ_e conversion can be implemented for currently available commercial RTP systems without any specialized modifications or extensions. Furthermore, the ΔHU–ρ_e conversion method only requires the ΔHU image data of the patient to be imported as if it were a conventional CT image, and a lookup table (LUT) is used for the ΔHU–ρ_e conversion as if it were an LUT for the HU–ρ_e conversion. The ΔHU image data of the patient should be generated from the measured dual-kV CT images using Eq. (1) with the weighting factor α determined in advance by scanning a calibration phantom. The author and colleagues previously presented the first implementation of the ΔHU–ρ_e conversion method for an RTP system and demonstrated its superior performance relative to that of the conventional HU–ρ_e conversion method in terms of the dose calculation accuracy [7].

2.2 Analytical photon-counting DECT-image simulations

2.2.1 Simulation framework

The procedure for the present analytical photon-counting DECT-image simulations is essentially the same as that used in the previous studies, except for the scan sequence and detection system [15]. Thus, only the aspects relevant to the present work will be described here. The photon-counting DECT-image simulation was performed as a single scan

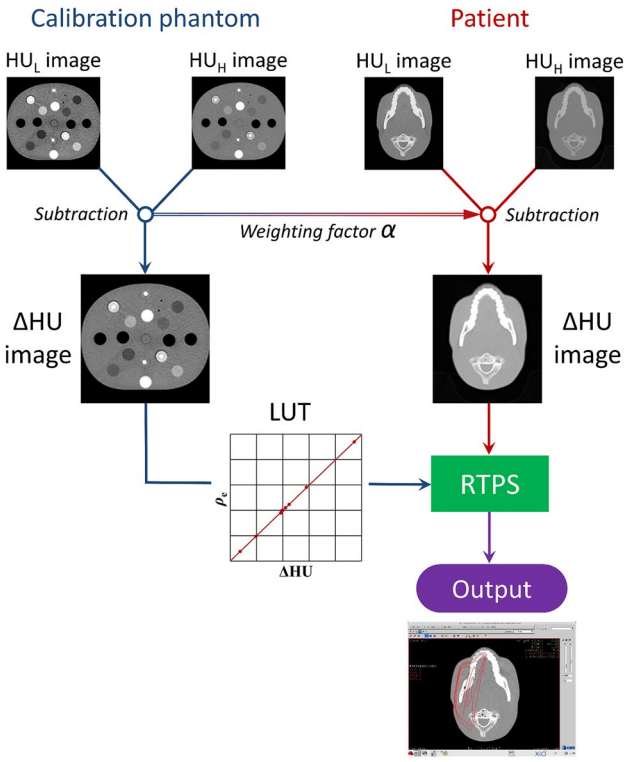

Fig. 1 Schematic workflow of the DECT-image-based RTP. The ΔHU image data of patients are generated from the measured dual-kV CT images using Eq. (1) with the weighting factor α determined in advance by scanning a calibration phantom. The lookup table (LUT) is also acquired from the DECT scanning of the calibration phantom. Subsequently, the ΔHU image data and the LUT for the ΔHU–ρ_e conversion are imported into an RTP system (RTPS) as if they were a conventional CT image and an LUT for HU–ρ_e conversion, respectively

with one tube voltage using a two-dimensional fan-beam geometry. The fan angle was set to approximately 34°. X-ray spectra were simulated for three different tube voltages: 120, 130, and 140 kV [16]. An aluminum bow-tie filter was taken into consideration. Its thickness, altered by the change of the beam angle, was computed according to the process described by Harpen [17]. Projections with 1800 views per 360° were analytically generated. Low- and high-energy images in a 512×512 matrix (0.68-mm pixel size) were reconstructed using a conventional filtered-backprojection algorithm with a Hann filter. No correction for beam hardening was performed, so that the impact of beam-hardening effects on the ΔHU–ρ_e conversion could be investigated. The analytical simulation program was coded by the author in FORTRAN language.

2.2.2 Photon-counting detector

A PCD was modeled as a direct-conversion CdTe semiconductor array. The ΔHU–ρ_e conversion can be inherently performed using multi-energy bins, and the increasing number of possible combinations of dual-energy bins may improve the ρ_e-image quality. As a first step, only two energy bins with two-sided windows were set in this study for simplicity: one was used to effectively simulate the high-energy scan, while the other was used for the low-energy scan. The mean detected signal S_i of the low-energy bin ($i=1$) or high-energy bin ($i=2$) at a PCD pixel can be expressed as follows:

$$S_i = \int B_i(E)\Phi_0(E)\mathrm{e}^{-\int_L \mu(E,x)\mathrm{d}x}Q(E)\mathrm{d}E, \tag{4}$$

where $\Phi_0(E)$ is the incident photon fluence per unit tube loading per unit energy for a monochromatic X-ray energy E, $\mu(E,x)$ is the linear attenuation coefficient at the object location x, and $Q(E)$ is the detector's quantum efficiency (assumed to be unity). $B_i(E)$ is the so-called bin sensitivity function, which can be estimated from the energy response of the detector. The nominal energy threshold, E_{th}, at the common boundary of two bins was treated as a variable parameter. The PCD was simulated for an ideal and a more realistic case [13]. Figure 2 shows an example of the calculated profiles of $B_i(E)\Phi_0(E)$ in Eq. (4) for two energy bins ($i=1, 2$) at 140 kV with $E_{th}=70$ keV. Note that these profiles do not represent the actual distributions of the pulse height of the signal generated by the detected photons; rather, they represent the energy distributions of those photons that can be counted in each energy bin. The upper panel spectra correspond to the ideal PCD case. The ideal PCD detects every photon at its correct energy. Therefore, in the ideal case, two energy bins are sharply separated at their common boundary E_{th}. In the realistic case, conversely, physical effects in the detection process limit the ability of the detector to resolve the true photon energy. To generate the spectral response of a realistic PCD, a phenomenological model proposed by Schlomka et al. [18] was implemented in the simulation. Schlomka et al. [18] measured the energy response of a CdTe detector array using the monochromatic radiation from a synchrotron facility under a low-flux condition, such that the degradation of the spectral response by pulse pileup was avoided [11, 12, 19]. Based on the experimentally acquired data, they constructed a phenomenological model of the energy-dependent detector response, which has a Gaussian distribution around the true photon energy, a second Gaussian distribution around the energy of the K-escape peak, and a nearly constant tail over low energies resulting from charge-sharing events. The lower panel spectra of Fig. 2 correspond to the realistic PCD case calculated using the detector-response model of Schlomka et al. The strong overlap between the energy bins in the realistic PCD case implies that the incomplete pulse signals generated from high-energy photons can be counted in the low-energy bin. We neglected pulse-pileup effects in the simulation.

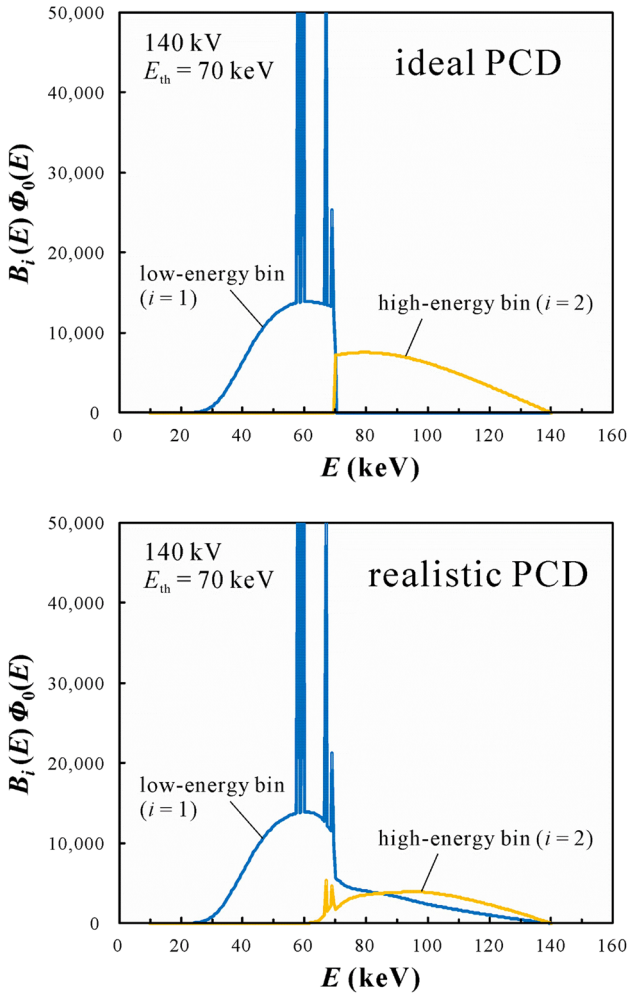

Fig. 2 Spectral profiles of $B_i(E)\Phi_0(E)$ in Eq. (4) for the low-energy ($i=1$) and high-energy ($i=2$) bins at 140 kV, with $E_{th}=70$ keV. Here, $\Phi_0(E)$ is the photon fluence of the central ray. The upper spectra are those for the ideal energy response of the PCD, and the lower spectra were obtained for the realistic energy-response case

2.2.3 Virtual phantoms

The photon-counting DECT-image simulations were used with two different types of virtual phantoms: a 35-cm-diameter pure water phantom (WP) and 33-cm-diameter solid water surrogate phantom (SWP) that simulated an electron-density calibration phantom, the Gammex 467 (Gammex, Middleton, Wisconsin) consisting of a Solid Water® disk. The SWP was equipped with 16 cylindrical inserts made of standard body tissues. The arrangement of the inserts in a solid water surrogate disk is schematically shown in Fig. 3. All objects are labelled with numbers, and their materials are listed in the figure. The elemental compositions of the body tissues and solid water surrogate were taken from ICRU Report no. 46 [20] and Bazalova et al. [21], respectively. Their mass attenuation coefficients were derived from the

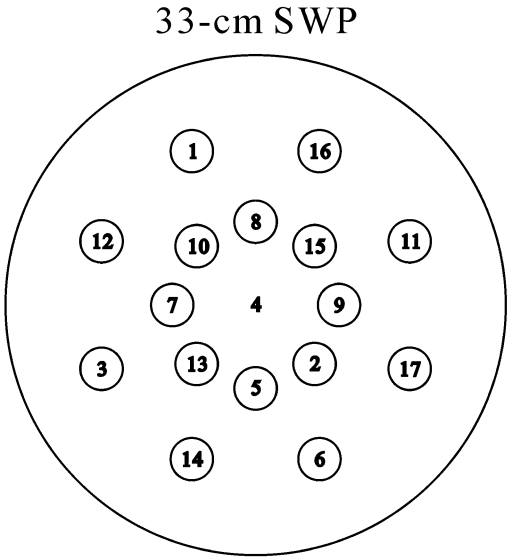

Fig. 3 Schematic of the arrangement of inserts in the 33-cm-diameter solid water surrogate phantom (SWP)

XCOM photon cross-sectional database [22]. In all image simulations, the SFOV was set to 35 cm.

2.2.4 CT dose index

The CT dose index (CTDI) from the exposure with the tube loading, quantified as the tube current–exposure time product (mAs), can be written as

$$\mathrm{CTDI} = \mathrm{mAs} \int \Phi_0(E)\theta(E)D(E)_{\mathrm{Mono}}\mathrm{d}E, \tag{5}$$

where $\theta(E)$ is the conversion factor of photon fluence to air kerma and $D(E)_{\mathrm{Mono}}$ is the CT dose coefficient over the entire diameter of the phantom per unit air kerma for a monochromatic X-ray energy E. In this study, the calculations of $D(E)_{\mathrm{Mono}}$ were performed for an infinitely long 35-cm-diameter cylindrical water tube with a body bow-tie filter for a 100-mm-length chamber using the dose computation tool reported by Zhou and Boone [23].

2.2.5 PCD performance metrics

The noise level and calibration accuracy in the resultant ρ_e^{cal} images were used as metrics for assessing the performance of the $\Delta\mathrm{HU}$–ρ_e conversion with an ideal or realistic PCD.

Figure 4 shows the workflow of the metric measurements. We measured the ρ_e-image noise, σ_e, at a fixed CTDI calculated using Eq. (5) in the circular region of interest (ROI) located at the center of the 35-cm-diameter WP. The value of α determined using the 33-cm-diameter SWP was also used here. Only statistical noise was added to each detected signal. The selection of the fixed CTDI can be arbitrary for the present purpose of spectral optimization, but we selected the CTDI value to attain a typical noise level of 1% (i.e., 10 HU standard deviations) in a 120-kV CT scan with a single energy bin covering the entire energy spectrum. To evaluate the accuracy, we measured ρ_e^{cal} values for 17 different circular ROIs located at the center of each insert in the SWP, following which we calculated the root-mean-square error (RMSE) between all the measured ρ_e^{cal} and true ρ_e values as follows:

$$\mathrm{RMSE} = \sqrt{\frac{1}{17}\sum_{j=1}^{17}\left(\rho_{ej}^{cal} - \rho_{ej}\right)^2}. \tag{6}$$

2.3 Proposal for improving ρ_e-calibration accuracy of realistic PCD

The performance degradation of the realistic PCD likely stems from the wide spectral spread outside E_{th} found in the low-energy bin (Fig. 2). As mentioned in Sect. 2.2.2, incomplete pulse signals generated from high-energy photons can be counted in the low-energy bin. Because this phenomenon is independent of the count rate and occurs at random times, the false signals in the low-energy bin should be proportional to the detected signals in the high-energy bin. Therefore, we would expect that the false counts in the low-energy bin can be removed, to a limited extent, by subtracting a portion of the high-energy signal (S_2) from the corresponding low-energy signal (S_1). The corrected low-energy signal for the image reconstruction, S_L, is expressed using Eq. (4) as follows:

$$\begin{aligned} S_L &= S_1 - \xi S_2 \\ &= \int \left\{B_1(E) - \xi B_2(E)\right\}\Phi_0(E)\mathrm{e}^{-\int_L \mu(E,x)\mathrm{d}x}Q(E)\mathrm{d}E, \end{aligned} \tag{7}$$

where ξ is the proportionality constant related to the fraction of high-energy photons detected in the low-energy bin.

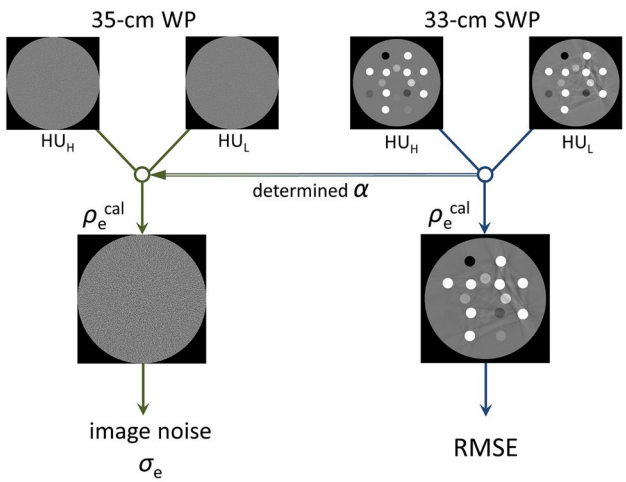

Fig. 4 Workflow of the metric measurements of the noise level and calibration accuracy in resultant ρ_e^{cal} images. We measured ρ_e^{cal}-image noise at a fixed CTDI, σ_e, in the circular ROI located at the center of the 35-cm-diameter water phantom (WP). The value of α determined using the 33-cm-diameter solid water surrogate phantom (SWP) was used here. To evaluate the calibration accuracy, we measured ρ_e^{cal} values for 17 different ROIs located at the center of each insert in the 33-cm-diameter SWP and then calculated the RMSE between all the measured and true ρ_e values

2.4 Effect of object size on ΔHU–ρ_e conversion

Ideally, the tube voltages, E_{th}, α, and ξ, are parameters that should be chosen for every patient according to body size to minimize the ρ_e-calibration errors. However, it is not an easy task to optimize these parameters from patient to patient, and the simplicity of the ΔHU–ρ_e conversion method would be lost with such optimization. Simplicity as well as accuracy with the use of a single set of parameters should be mandatory for achieving a standard of ρ_e calibration that can be routinely practiced in RTP. Therefore, a sufficient invariance in the ρ_e calibration based on a single parameter set is required against the change in object size. To investigate the effect of object size on the accuracy of the ΔHU–ρ_e conversion, CT images were simulated using another virtual phantom as the object. The object used here was essentially the same as the 33-cm-diameter calibration SWP, but the diameter of the solid water surrogate disk was reduced from 33 to 25 cm. The values of the tube voltage, E_{th}, α, and ξ, along with the 35-cm-diameter SFOV, which may be appropriate for the 33-cm-diameter SWP, were intentionally used for the 25-cm-diameter SWP as well. The use of the different-sized object with the inappropriate choice of SFOV was expected to induce a certain variation in the ρ_e^{cal} values as a result of beam-hardening effects.

3 Results

3.1 Examples of ΔHU–ρ_e conversion for ideal and realistic PCD cases

Representative examples of the ΔHU–ρ_e conversion for ideal and realistic PCD cases are described in this section. Figure 5 shows conventional HU–ρ_e plots for the

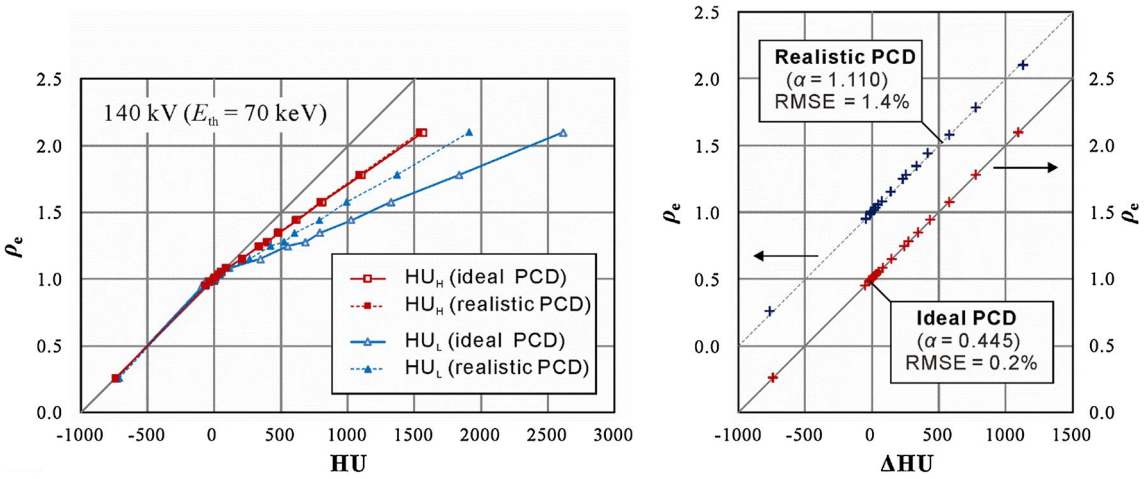

Fig. 5 HU–ρ_e plots of the 33-cm-diameter SWP for low-energy and high-energy bins, at a tube voltage of 140 kV, with E_{th} = 70 keV, for the ideal and realistic PCD cases. The resultant ΔHU–ρ_e plots for the ideal and realistic PCD cases are shown on the right side of the figure. The coordinates for the realistic PCD data were shifted upward by 0.5 to avoid overlap

33-cm-diameter SWP, for both low-energy and high-energy bins, at a tube voltage of 140 kV with E_{th} = 70 keV. This E_{th} value is almost at the midpoint of the 140-kV spectrum. Plots for the two scenarios of the ideal and realistic PCDs are included in this figure. The numerical data for ρ_e, HU_k (k = H, L), and ρ_e^{cal} fitted to the data obtained using the linear function of Eq. (2) are listed in Table 1, along with the deviations between ρ_e^{cal} and ρ_e, with various materials inserted in the 33-cm-diameter SWP for the ideal and realistic PCD cases. It is apparent that the CT number difference for each material between low- and high-energy bins was rather less distinct for the realistic PCD case than for the ideal case, suggesting a relatively poor separation of the dual-energy spectra in the realistic case. The resultant ΔHU–ρ_e plots are shown on the right side of Fig. 5. The weighting factors, α, which were determined using the 33-cm-diameter SWP, were 0.445 for the ideal case and 1.110 for the realistic case. For the ideal PCD, an excellent linear relationship between ΔHU and ρ_e was observed, with all of the ΔHU–ρ_e data points falling nearly on a straight line; for example,

Table 1 Simulated HU_H, HU_L, and ρ_e^{cal} values of materials inserted in the 33-cm-diameter SWP in the ideal PCD and realistic PCD cases at 140 kV with E_{th} = 70 keV. Deviations between ρ_e^{cal} and ρ_e are also given, along with the resulting values of RMSE calculated from Eq. (6)

No.	Material	ρ_e	Ideal PCD (α = 0.445)				Realistic PCD (α = 1.110)			
			HU_H	HU_L	ρ_e^{cal}	Dev. (%)	HU_H	HU_L	ρ_e^{cal}	Dev. (%)
1	Lung (inflated)	0.258	−734.6	−724.9	0.261	0.3	−734.1	−707.8	0.237	−2.1
2	Adipose	0.951	−61.9	−88.3	0.950	−0.1	−61.3	−75.5	0.954	0.3
3	Yellow marrow	0.982	−32.3	−62.9	0.981	−0.1	−31.7	−47.4	0.986	0.4
4	Solid water	0.990	−7.2	−1.5	0.990	0.0	−7.4	−8.6	0.994	0.4
5	Water	1.000	1.0	4.6	0.999	−0.1	1.0	7.4	0.994	−0.6
6	Breast	1.014	7.8	−6.1	1.014	0.0	8.1	0.6	1.016	0.2
7	Brain	1.035	36.3	41.6	1.034	−0.1	36.3	40.7	1.031	−0.4
8	Eye lens	1.055	52.8	52.4	1.053	−0.2	53.0	59.0	1.046	−0.9
9	Cartilage	1.083	92.3	113.8	1.083	0.0	91.8	103.8	1.079	−0.4
10	Spongiosa	1.150	210.8	348.7	1.149	−0.1	207.8	265.8	1.143	−0.7
11	Sacrum	1.246	337.9	552.2	1.243	−0.3	333.3	425.3	1.231	−1.5
12	Femur	1.278	401.9	687.1	1.275	−0.3	396.0	523.7	1.254	−2.4
13	Ribs (2nd, 6th)	1.347	484.1	791.0	1.348	0.1	477.4	605.0	1.336	−1.1
14	Ribs (10th)	1.441	620.5	1030.2	1.438	−0.3	611.9	788.0	1.416	−2.5
15	Mandible	1.577	810.6	1327.1	1.581	0.4	798.8	994.3	1.582	0.5
16	Cortical bone	1.781	1106.8	1840.2	1.781	0.0	1090.6	1373.7	1.776	−0.5
17	Uri. stones oxal.	2.099	1566.8	2617.3	2.100	0.1	1542.9	1914.7	2.130	3.1
			RMSE (%) = 0.2				RMSE (%) = 1.4			

the maximal deviation between ρ_e^{cal} and ρ_e was 0.4% for the mandible insert. The resulting RMSE calculated from Eq. (6) was 0.2%. Conversely, the ΔHU–ρ_e data points for the realistic case appeared to deviate slightly from a straight line. The maximal ρ_e^{cal} deviation was 3.1% for the urinary-stones-oxalate insert, which resulted in RMSE = 1.4%.

3.2 Spectral optimization

To determine the optimal values of E_{th} and tube voltage, which are spectral parameters, we evaluated the accuracy for ρ_e calibration, as in the example above, by varying E_{th} from 40 keV up to 130 keV. Figure 6a shows the variations of the weighting factor α for the ideal case as a function of E_{th} at tube voltages of 120, 130, and 140 kV. The α values at a fixed tube voltage were almost steady with respect to the variation in E_{th} for E_{th} values above 60 keV, which corresponds to energies greater than that of the characteristic Kα X-ray from a tungsten target. As the tube voltage increased, the overall values of α decreased, indicating that a larger tube voltage leads to a larger spectral separation between the dual-energy bins. Figure 6b shows the variation in the ρ_e^{cal}-image noise for the 35-cm-diameter WP, σ_e. The minima in the downward convex curves of σ_e appeared for the respective tube voltages. Among them, the lowest σ_e was achieved at 140 kV with E_{th} = 60 keV (1.9%), although the minimum for the σ_e curve was very shallow. The corresponding plots of RMSE are given in Fig. 6c. Individual minima in the RMSE for every tube voltage appeared at ~ 70 keV, and the lowest RMSE was 0.2% for 140 kV. The σ_e value at 140 kV with E_{th} = 70 keV was 2.0%, which is nearly equal to the lowest σ_e. Considering these circumstances, a tube voltage of 140 kV with E_{th} = 70 keV would be optimal in the ideal PCD case, because it simultaneously yields approximate minima for RMSE and σ_e.

The corresponding plots for the realistic case as a function of E_{th} are summarized in Fig. 7. The related plots for the ideal case at its optimal tube voltage of 140 kV, which have already been given in Fig. 6, are overlaid in each figure for comparison. As shown in Fig. 7a, the variations in α in the realistic case exhibit a different behavior from that in the ideal case. Accordingly, the values of α at the respective tube voltages decreased with increasing E_{th}. The values of α were always significantly higher than those for the ideal case, suggesting that the spectral profiles of high- and low-energy bins are poorly separated in the realistic case. Figure 7b shows the variation in σ_e. Individual minima are observed at 70 keV for every tube voltage. The lowest σ_e was 3.7%, which was achieved at 140 kV, and it was approximately twice that of the ideal case. Corresponding plots of RMSE are given in Fig. 7c. A higher E_{th} yielded, in general, a low RMSE value; furthermore, no minima appeared. As demonstrated for the ideal case, an optimal E_{th} would provide both the lowest RMSE and the lowest σ_e. Unfortunately, this does not occur in the realistic case. RMSEs can barely reach a level below 1% using $E_{th} \geq 110$ keV at the expense of substantially increased image noise (at least, σ_e = 6.0% for 140 kV). Such an inferior performance in the ρ_e calibration may not be practically acceptable.

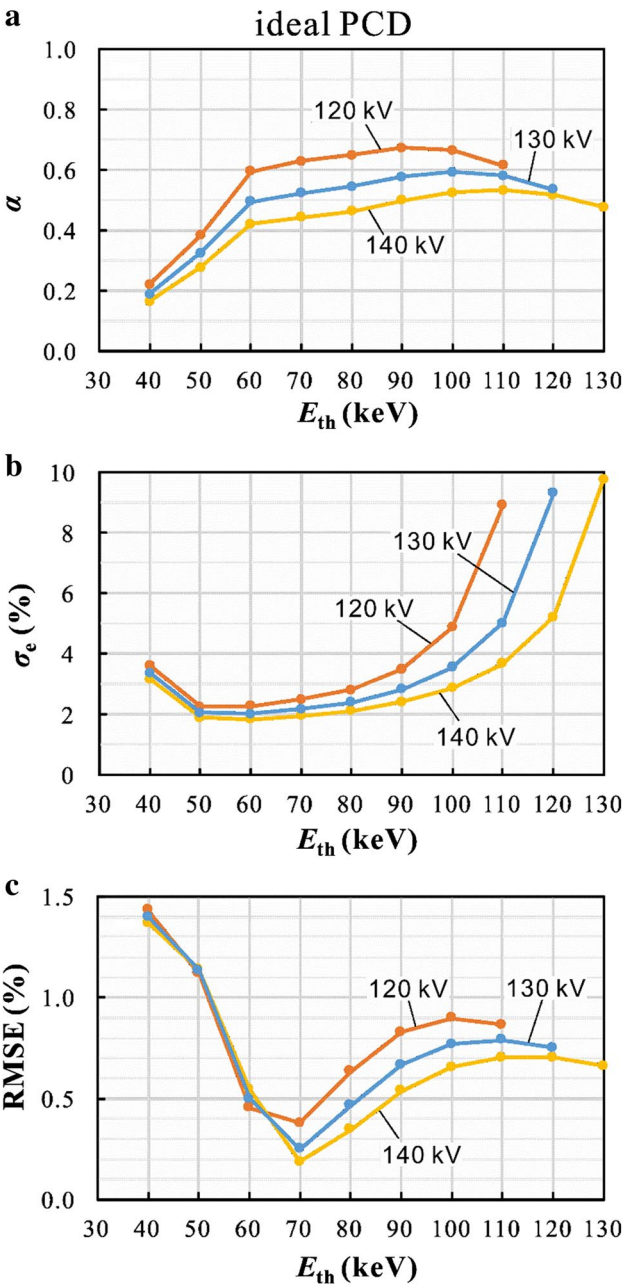

Fig. 6 Variations of **a** weighting factor α, **b** ρ_e^{cal}-image noise σ_e, and **c** ρ_e^{cal}-calibration errors of RMSE for the ideal PCD case, as a function of E_{th}, for three tube voltages: 120, 130, and 140 kV

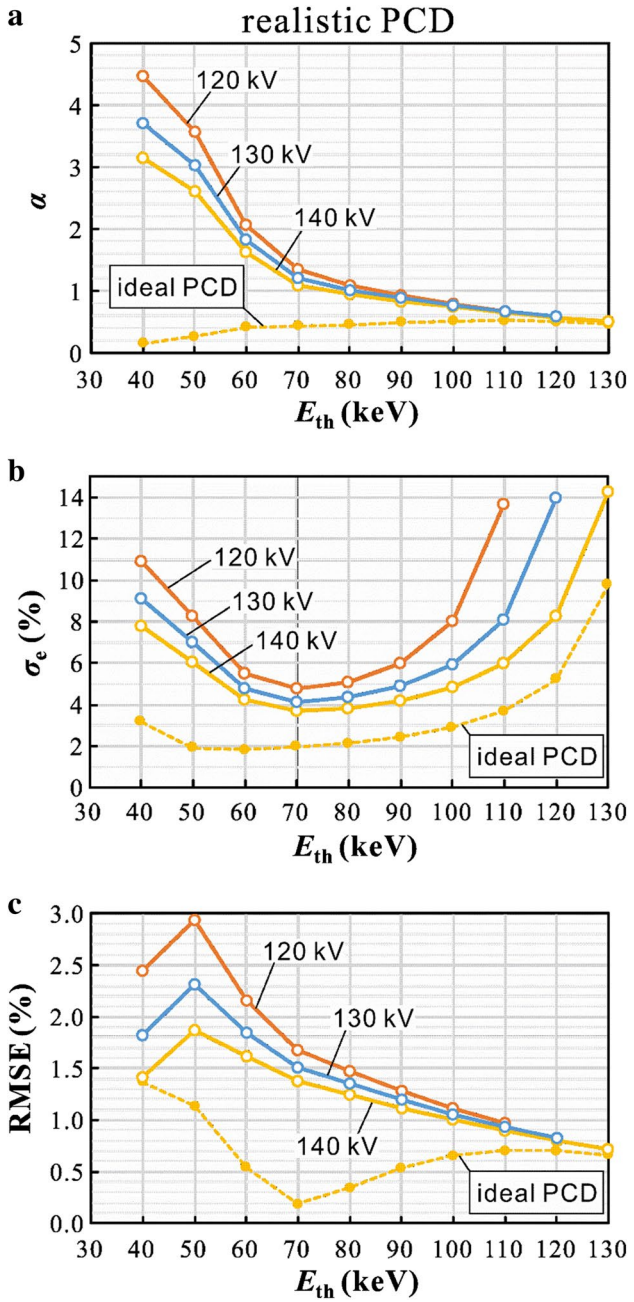

Fig. 7 Variations of **a** weighting factor α, **b** ρ_e^{cal}-image noise σ_e, and **c** ρ_e^{cal}-calibration errors of RMSE for the realistic PCD case, as a function of E_{th}, for three tube voltages: 120, 130, and 140 kV. The corresponding plots for the ideal case at its optimal tube voltage of 140 kV are overlaid in each figure for comparison

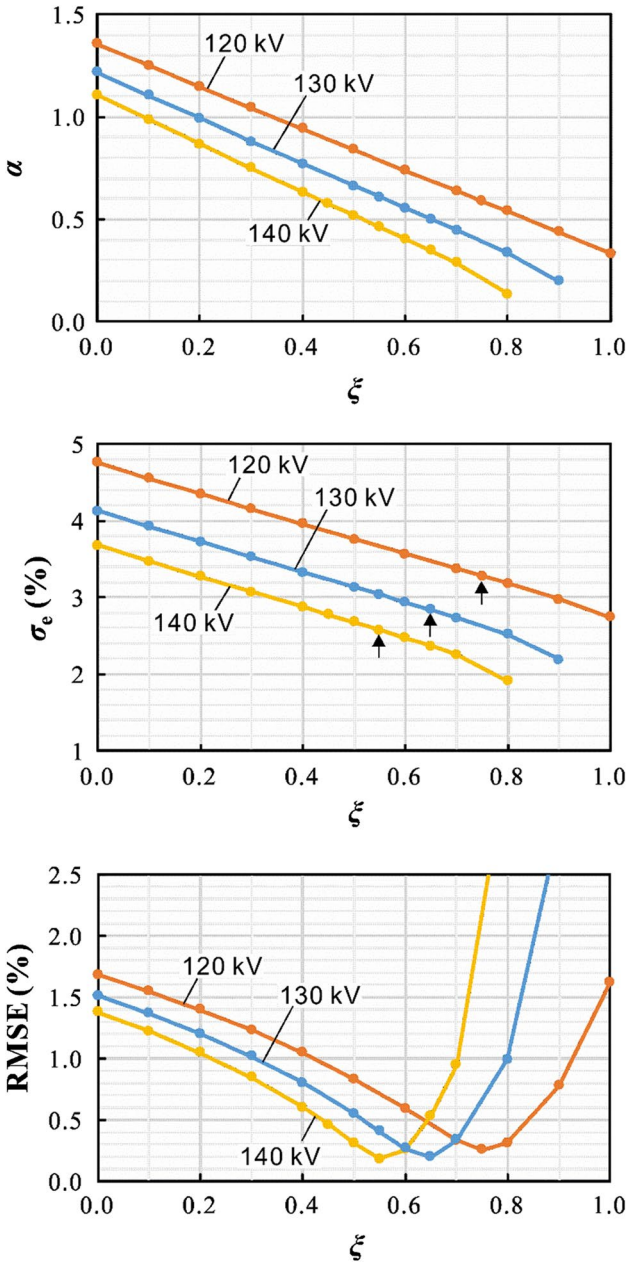

Fig. 8 Variations of **a** weighting factor α, **b** ρ_e^{cal}-image noise σ_e, and **c** ρ_e^{cal}-calibration errors of RMSE for the realistic PCD case, as a function of the proportionality constant ξ in Eq. (7), for three tube voltages (120, 130, and 140 kV), for $E_{th} = 70$ keV

3.3 Improved spectral separation of realistic PCD

The poor spectral separation of a realistic PCD can be improved by subtracting a portion of the high-energy signal from the corresponding low-energy signal. Figure 8a shows the variation in α as a function of ξ in Eq. (7) at tube voltages of 120, 130, and 140 kV for the realistic PCD case. Here, the value of E_{th} was always set to 70 keV, which provided the lowest RMSE for every tube voltage in the ideal case. It was found that α decreased with increasing ξ, indicating that a larger ξ leads to a stronger spectral separation between the high- and low-energy bins, as expected. As shown in Fig. 8b, the corresponding value of σ_e also decreased monotonically with increasing ξ. Figure 8c shows the variations in RMSE. The increase in ξ led to a significant reduction in RMSE and enabled the determination of individual minima at a certain

value of ξ. Although the value of ξ that minimizes RMSE varies according to the tube voltage ($\xi=0.75$ for 120 kV, $\xi=0.65$ for 130 kV, and $\xi=0.55$ for 140 kV), the minimal attainable RMSE values were almost the same (0.2%). A tube voltage of 140 kV ($E_{th}=70$ keV) with $\xi=0.55$ would be optimal, because it yields the lowest image noise ($\sigma_e=2.6\%$), as indicated by the arrows in Fig. 8b. Figure 9 shows the resultant low-energy spectrum of $\{B_1(E)-\xi B_2(E)\}\Phi_0(E)$ in Eq. (7), corrected under the optimal condition of $\xi=0.55$ at 140 kV with $E_{th}=70$ keV, along with the high-energy spectrum multiplied by $\xi=0.55$. The uncorrected low-energy spectrum (i.e., $\xi=0$) is overlaid for comparison. The wide spread outside E_{th} observed for the low-energy bin was considerably reduced in the corrected case compared with that of the uncorrected case, although the overlap between the energy bins was not completely absent, as in the ideal case.

3.4 Effect of object size

To investigate the effect of object size on the accuracy of the ΔHU–ρ_e conversion, CT images were simulated using the 25-cm-diameter SWP as the object. Figure 10a–c shows the plots of HU–ρ_e simulated for three cases: the ideal PCD, realistic PCD, and realistic PCD corrected with $\xi=0.55$, respectively. The corresponding HU–ρ_e plots simulated using the 33-cm-diameter SWP are overlaid on each graph for comparison. For the three PCD cases, Table 2 lists numerical data for ρ_e, HU_k (k=H, L), and ρ_e^{cal} for the materials inserted in the 25-cm-diameter SWP. In Fig. 10b, we were able to identify relatively large horizontal shifts in HU_L for the realistic PCD case. The ΔHU–ρ_e plots for the 25-cm-diameter and 33-cm-diameter SWPs are shown on the right side of each figure. For the ideal PCD, a good linear relationship between ΔHU and ρ_e was achieved again with the 25-cm-diameter SWP, and all of the ΔHU–ρ_e data points fell nearly on a straight line; for example, the maximal deviation between ρ_e^{cal} and ρ_e was 1.7% for the urinary-stones-oxalate insert, resulting in RMSE = 0.6%. Although the deviations were somewhat greater than those in the 33-cm-diameter SWP case because of the change in the object size, it may safely be asserted that most of the deviations were within ± 1.0%. Conversely, the ΔHU–ρ_e data points for the realistic case deviated significantly from a straight line. The maximal ρ_e^{cal} deviations were −7.9% for the cortical bone, resulting in RMSE = 3.8%, which was approximately three times greater than the result for the 33-cm-diameter SWP (1.4%). As with the case of the 33-cm-diameter SWP, however, the proposed correction of the low-energy signal with $\xi=0.55$ allowed a significant reduction of the RMSE of the 25-cm-diameter SWP to 0.7% for the ideal case (0.6%).

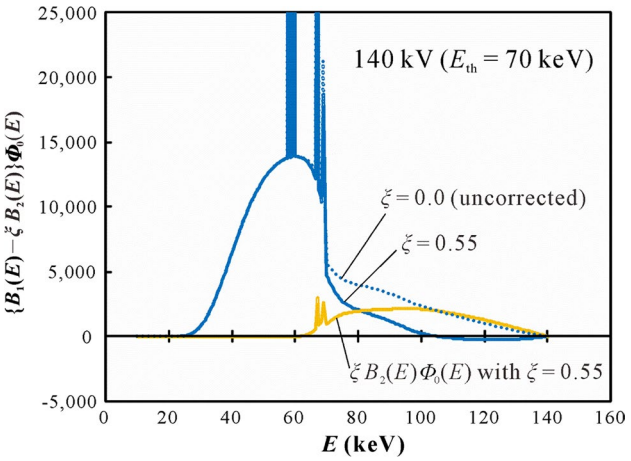

Fig. 9 Resultant low-energy spectrum corrected under the optimal condition of $\xi=0.55$ at 140 kV with $E_{th}=70$ keV, along with the high-energy spectrum multiplied by $\xi=0.55$. The uncorrected low-energy spectrum (i.e., $\xi=0$) is overlaid for comparison

4 Discussion

Faby et al. [13] previously reported a simulation study using the scenarios of ideal and realistic PCDs to characterize the energy response of a detector with respect to the performance of PCDs for other DECT applications: virtual non-contrast imaging and iodine quantification. They found noticeable improvements in the material image quality for an ideal PCD; however, the prediction for a realistic PCD has little use for the material decomposition task. To compensate for its performance losses, they proposed a new concept of DSCT equipped with both a PCD and a conventional energy-integrated detector. In the present study, an alternative and simple method is proposed for improving the accuracy of the ΔHU–ρ_e conversion for a realistic PCD. Figure 11 summarizes the performances of three PCD cases: the ideal PCD, realistic PCD, and realistic PCD corrected with $\xi=0.55$. The present correction of the low-energy signal is observed to improve the performance of the realistic PCD significantly to a level comparable with the ideal case in terms of the α and RMSE values. Unfortunately, the image noise σ_e (2.6%) is greater than that in the ideal case (2.0%) because of the subtraction process given in Eq. (7). However, the marked reduction of α from 1.110 to 0.462 allowed for a smaller σ_e than that obtained in the realistic PCD case without correction (3.7%).

A comparison of ρ_e^{cal} images for the 25-cm-diameter SWP for the three PCD cases is shown in Fig. 12, along with their high- and low-energy CT images. Beam-hardening-induced streaking artifacts can be observed among the higher density inserts, particularly for all the low-energy CT images. It should be stressed that these artifacts are caused by spectral hardening as a result of the detector resolution effects; this is different from the "conventional" beam-hardening

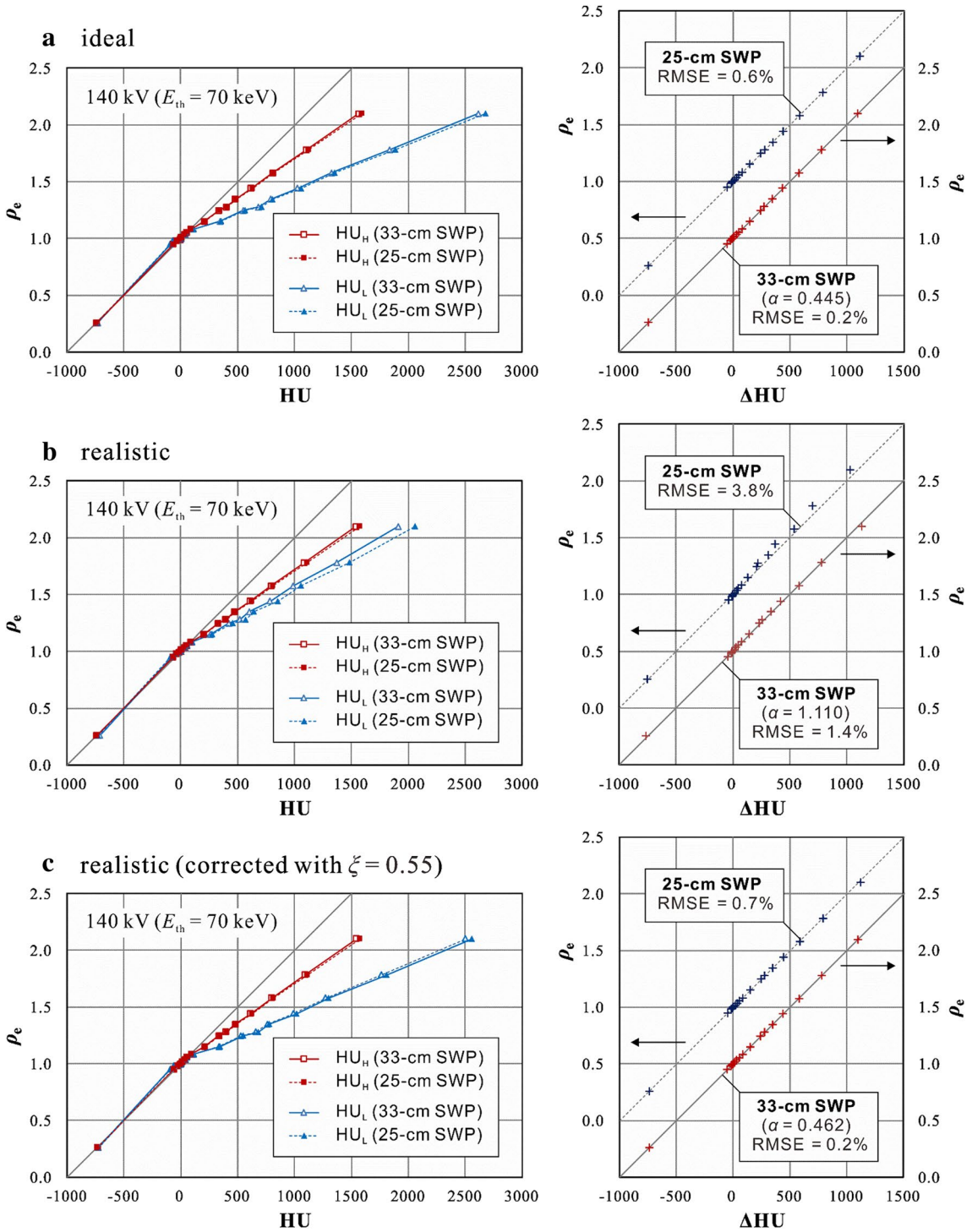

Fig. 10 HU–ρ_e plots for the 25-cm-diameter SWP, for low-energy and high-energy bins, at a tube voltage of 140 kV, with E_{th} = 70 keV, for the three cases: **a** ideal PCD, **b** realistic PCD, and **c** realistic PCD corrected with ξ = 0.55. The corresponding HU–ρ_e plots simulated using the 33-cm-diameter SWP are overlaid in each graph for comparison. The resultant ΔHU–ρ_e plots for the 25-cm-diameter and 33-cm-diameter SWPs are shown on the right side of each figure. The coordinates for the 25-cm-diameter SWP data were shifted upward by 0.5 to avoid overlap

Table 2 Simulated HU_H, HU_L, and ρ_e^{cal} values of materials inserted in the 25-cm-diameter SWP at 140 kV with $E_{th}=70$ keV for an ideal PCD, realistic PCD, and realistic PCD with correction ($\xi=0.55$)

No.	Material	ρ_e	Ideal PCD ($\alpha=0.445$)				Realistic PCD ($\alpha=1.110$)				Realistic PCD with correction ($\alpha=0.462$, $\xi=0.55$)			
			HU_H	HU_L	ρ_e^{cal}	Dev. (%)	HU_H	HU_L	ρ_e^{cal}	Dev. (%)	HU_H	HU_L	ρ_e^{cal}	Dev. (%)
1	Lung (inflated)	0.258	−736.6	−731.2	0.261	0.3	−736.2	−720.1	0.246	−1.2	−736.2	−731.0	0.261	0.3
2	Adipose	0.951	−62.2	−93.8	0.952	0.1	−61.7	−83.3	0.962	1.1	−61.7	−91.7	0.952	0.1
3	Yellow marrow	0.982	−31.3	−66.1	0.984	0.2	−30.6	−50.0	0.991	0.9	−30.6	−63.7	0.985	0.3
4	Solid water	0.990	−6.8	−4.8	0.992	0.2	−7.0	−11.9	0.999	0.9	−7.0	−6.1	0.993	0.3
5	Water	1.000	1.6	3.3	1.001	0.1	1.7	6.6	0.996	−0.4	1.7	3.3	1.001	0.1
6	Breast	1.014	9.5	−7.4	1.017	0.3	9.8	1.8	1.019	0.5	9.8	−6.6	1.017	0.3
7	Brain	1.035	37.2	40.8	1.036	0.1	37.2	41.1	1.033	−0.2	37.2	40.3	1.036	0.1
8	Eye lens	1.055	53.6	52.1	1.054	−0.1	53.9	59.7	1.047	−0.8	53.9	52.7	1.054	−0.1
9	Cartilage	1.083	93.5	114.0	1.084	0.1	93.2	106.3	1.079	−0.4	93.2	111.9	1.085	0.2
10	Spongiosa	1.150	214.7	356.3	1.152	0.2	211.9	283.2	1.133	−1.7	211.9	341.3	1.152	0.2
11	Sacrum	1.246	345.7	568.6	1.247	0.1	341.7	462.7	1.207	−3.9	341.7	545.6	1.247	0.1
12	Femur	1.278	411.5	709.6	1.279	0.1	406.2	572.6	1.222	−5.6	406.2	680.1	1.280	0.2
13	Ribs (2nd, 6th)	1.347	492.1	810.2	1.351	0.4	485.8	646.0	1.308	−3.9	485.8	777.2	1.351	0.4
14	Ribs (10th)	1.441	633.7	1061.3	1.444	0.3	625.7	855.8	1.370	−7.1	625.7	1017.9	1.444	0.3
15	Mandible	1.577	823.5	1356.8	1.586	0.9	812.2	1059.7	1.538	−3.9	812.2	1298.8	1.587	1.0
16	Cortical bone	1.781	1128.9	1888.6	1.791	1.0	1113.6	1484.9	1.702	−7.9	1113.6	1806.1	1.793	1.2
17	Uri. stones oxal.	2.099	1597.3	2679.8	2.116	1.7	1574.5	2063.8	2.032	−6.7	1574.5	2556.8	2.120	2.1
			RMSE (%) = 0.6				RMSE (%) = 3.8				RMSE (%) = 0.7			

Deviations between ρ_e^{cal} and ρ_e are also given, along with the resulting values of RMSE calculated from Eq. (6)

effect caused by energy-dependent attenuation inside the object. In the ρ_e^{cal} image for the ideal PCD case, the artifacts were almost completely eliminated by compensating for the beam-hardening effects between the dual-energy CT images, even though no beam-hardening correction was performed. Conversely, the artifacts remained in the ρ_e^{cal} image for the realistic PCD case. For the realistic PCD case with the correction of $\xi=0.55$, however, the artifacts were suppressed to a level comparable with that for the ideal PCD case, as expected. Thus, the present correction method seems to enable a considerable improvement in the image quality of the realistic PCD for the ΔHU–ρ_e conversion, even for ill-conditioned scans in which the sizes of the patient and calibration SWP do not match. Nevertheless, further research by simulating CT images of more highly anisotropic and heterogeneous objects may be needed to confirm the invariance in the ρ_e calibration based on a single ξ parameter.

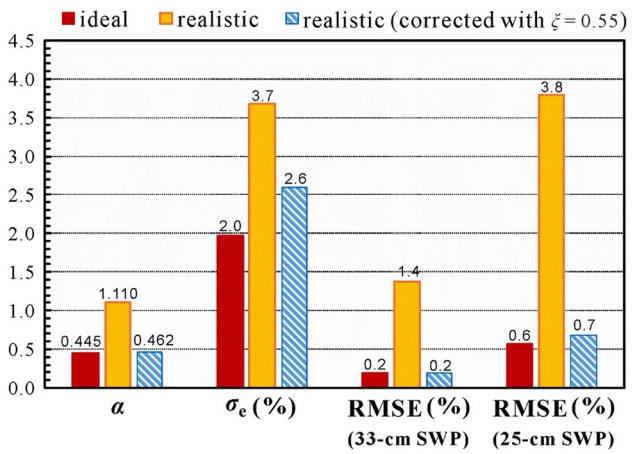

Fig. 11 Comparison of the performances (α, σ_e, RMSEs for 33-cm-diameter and 25-cm-diameter SWPs), for the three cases: ideal PCD, realistic PCD, and realistic PCD corrected with $\xi=0.55$ at 140 kV with $E_{th}=70$ keV

One limitation of this study is that pulse pileup was not taken into consideration. Pulse pileup is a count-rate-dependent phenomenon, and currently available PCDs suffer from the most substantial issue, which is the inability to handle high-count rates encountered in clinical CT. Furthermore, we did not include crosstalk caused by the charge drift in neighboring pixels that exists in currently used PCDs. These problems cannot be resolved using the correction method proposed in this work. In addition, we neglected scattering in the CT image simulation. Increasing the object's size would increase the scattering and thereby contribute to the degradation of image quality. Therefore, the results for the corrected realistic PCD presented here should be interpreted as an upper bound on performance.

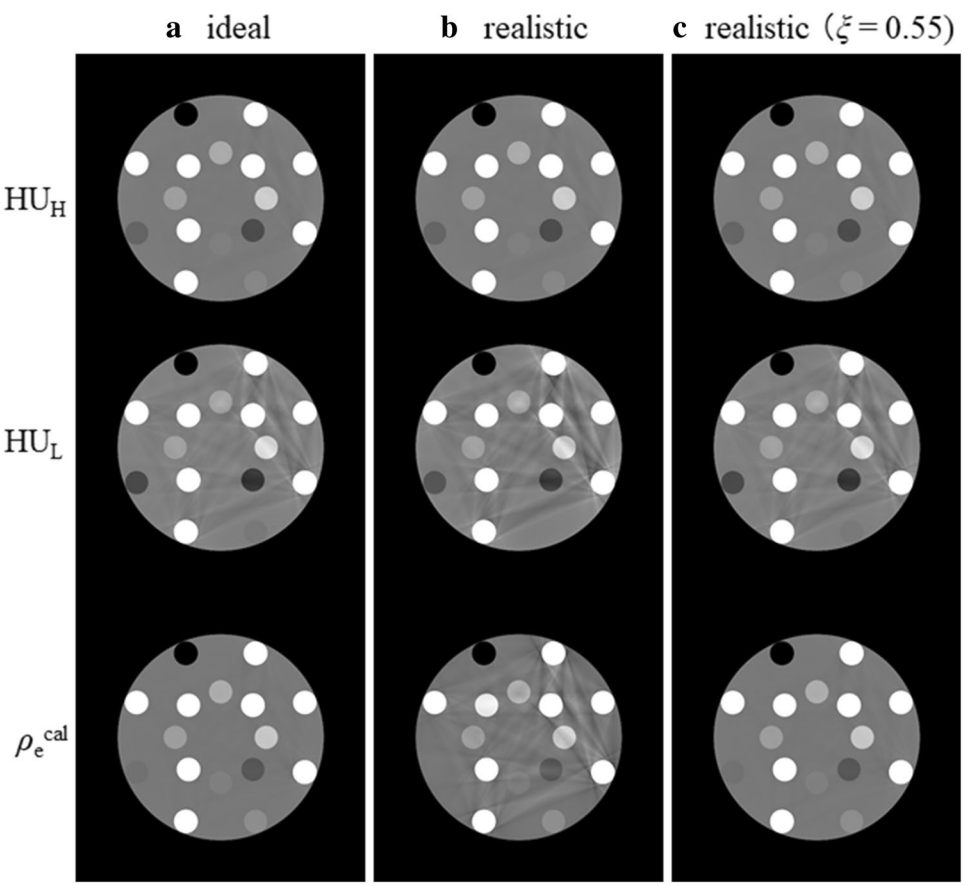

Fig. 12 Comparison of simulated high-energy and low-energy CT images of 25-cm-diameter SWP (WL = 0 HU, WW = 300 HU), and the resultant ρ_e^{cal} images (WL = 1.0, WW = 0.3), at 140 kV, with $E_{th} = 70$ keV, for the three cases: **a** ideal PCD, **b** realistic PCD, and **c** realistic PCD corrected with $\xi = 0.55$

5 Conclusion

This paper described a spectral optimization technique for an energy-selective PCD used for the ΔHU–ρ_e conversion. Within the limits of validity of the analytical simulation in this work, the optimal E_{th} of the ideal PCD was found to be 70 keV at a tube voltage of 140 kV, because this value yielded lower σ_e and RMSE values. Physical effects occurring in realistic PCDs unfortunately deteriorate the expected PCD performance. However, the proposed correction method for improving the spectral separation could potentially improve the performance of realistic PCDs to a level comparable with that of the ideal case in terms of the accuracy of the resultant ρ_e^{cal}. The improved spectral separation was clearly reflected in the simulated ρ_e^{cal} images, with less distinct beam-hardening artifacts. However, to fully investigate the ρ_e-calibration accuracy of the ΔHU–ρ_e conversion using PCDs, further research is required that would account for the effects of pulse pileup, crosstalk, and scattering, which were ignored in the present study.

Acknowledgements This work was supported in part by JSPS KAKENHI Grant number 16K09011.

Compliance with ethical standards

Conflict of interest The author has no conflicts of interest to disclose.

Ethical statement This article does not contain any studies with human participants or animals performed.

Informed consent Informed consent is not required.

References

1. Parker RP, Hobday PA, Cassell KJ. The direct use of CT numbers in radiotherapy dosage calculations for inhomogeneous media. Phys Med Biol. 1979;24(4):802–9.
2. Constantinou C, Harrington JC, DeWerd LA. An electron density calibration phantom for CT-based treatment planning computers. Med Phys. 1992;19(2):325–7.
3. Schneider U, Pedroni E, Lomax A. The calibration of CT Hounsfield units for radiotherapy treatment planning. Phys Med Biol. 1996;41(1):111–24.
4. du Plessis FCP, Willemse CA, Lotter MG, Goedhals L. The indirect use of CT numbers to establish material properties needed for Monte Carlo calculation of dose distributions in patients. Med Phys. 1998;25(7):1195–201.

5. Saito M. Potential of dual-energy subtraction for converting CT numbers to electron density based on a single linear relationship. Med Phys. 2012;39(4):2021–30.
6. Tsukihara M, Noto Y, Hayakawa T, Saito M. Conversion of the energy-subtracted CT number to electron density based on a single linear relationship: an experimental verification using a clinical dual-source CT scanner. Phys Med Biol. 2013;58(9):N135–44.
7. Tsukihara M, Noto Y, Sasamoto R, Hayakawa T, Saito M. Initial implementation of the conversion from the energy-subtracted CT number to electron density in tissue inhomogeneity corrections: an anthropomorphic phantom study of radiotherapy treatment planning. Med Phys. 2015;42(3):1378–88.
8. Landry G, Parodi K, Wildberger JE, Verhaegen F. Deriving concentrations of oxygen and carbon in human tissues using single- and dual-energy CT for ion therapy applications. Phys Med Biol. 2013;58(15):5029–48.
9. Hünemohr N, Krauss B, Tremmel C, Ackermann B, Jäkel O, Greilich S. Experimental verification of ion stopping power prediction from dual energy CT data in tissue surrogates. Phys Med Biol. 2014;59(1):83–96.
10. Primak AN, Giraldo JCR, Liu X, Yu L, McCollough CH. Improved dual-energy material discrimination for dual-source CT by means of additional spectral filtration. Med Phys. 2009;36(4):1359–69.
11. Taguchi K, Iwanczyk JS. Vision 20/20: Single photon counting X-ray detectors in medical imaging. Med Phys. 2013;40(10):100901.
12. Taguchi K. Energy-sensitive photon counting detector-based X-ray computed tomography. Radiol Phys Technol. 2017;10(1):8–22.
13. Faby S, Kuchenbecker S, Sawall S, Simons D, Schlemmer H-P, Lell M, Kachelrieß M. Performance of today's dual energy CT and future multi energy CT in virtual non-contrast imaging and in iodine quantification: a simulation study. Med Phys. 2015;42(10):4349–66.
14. Saito M, Tsukihara M. Technical Note: Exploring the limit for the conversion of energy-subtracted CT number to electron density for high-atomic-number materials. Med Phys. 2014;41(7):071701.
15. Saito M. Optimized low-kV spectrum of dual-energy CT equipped with high-kV tin filtration for electron density measurements. Med Phys. 2011;38(6):2850–8.
16. Cranley K, Gilmore BJ, Fogarty GWA, Deponds L. Catalog of diagnostic X-ray spectra and other data (IPEM report no. 78). York: IPEM Publications; 1997.
17. Harpen MD. A simple theorem relating noise and patient dose in computed tomography. Med Phys. 1999;26(11):2231–4.
18. Schlomka JP, Roessl E, Dorscheid R, Dill S, Martens G, Istel T, Bäumer C, Herrmann C, Steadman R, Zeitler G, Livne A, Proksa R. Experimental feasibility of multi-energy photon-counting *K*-edge imaging in pre-clinical computed tomography. Phys Med Biol. 2008;53(15):4031–47.
19. Cammin J, Xu J, Barber WC, Iwanczyk JS, Hartsough NE, Taguchi K. A cascaded model of spectral distortions due to spectral response effects and pulse pileup effects in a photon-counting X-ray detector for CT. Med Phys. 2014;41(4):041905.
20. International Committee on Radiation Units and Measurements. Photon, electron, proton, and neutron interaction data for body tissues (ICRU Report 46), Bethesda; 1992.
21. Bazalova M, Carrier J-F, Beaulieu L, Verhaegen F. Dual-energy CT-based material extraction for tissue segmentation in Monte Carlo dose calculations. Phys Med Biol. 2008;53(9):2439–56.
22. Berger MJ, Hubbell JH. XCOM: photon cross-sections on a personal computer. Gaithersburg: NBSIR; 1987. pp. 87–3597.
23. Zhou H, Boone JM. Monte Carlo evaluation of $CTDI_{\infty}$ in infinitely long cylinders of water, polyethylene and PMMA with diameters from 10 mm to 500 mm. Med Phys. 2008;35(6):2424–31.